Supercritical "boiling" number, a new parameter to distinguish two regimes of carbon dioxide heat transfer in tubes

Bingguo Zhu[a], Jinliang Xu[a,*], Xinming Wu[a], Jian Xie[a,**], Mingjia Li[b]

[a] The Beijing Key Laboratory of Multiphase Flow and Heat Transfer, North China Electric Power University, Beijing, 102206, Beijing, China
[b] Key Laboratory of Thermo-Fluid Science and Engineering of Ministry of Education, School of Energy & Power Engineering, Xi'an Jiaotong University, Xi'an, Shanxi, 710049, China

ABSTRACT

The objective of this paper is to develop a criterion to predict the onset of heat transfer deterioration (HTD) for supercritical CO_2 heat transfer. A new mechanism is proposed by assuming supercritical pseudo-boiling. Before bulk fluid reaches pseudo-critical temperature (T_{pc}), the tube cross-section contains a vapor layer and a liquid-like fluid. The saturation temperature interface is defined at $T = T_{pc}$, inside and outside which are a vapor layer ($T > T_{pc}$) and a subcooled liquid ($T < T_{pc}$). The subcritical boiling number is extended to supercritical "boiling" number, defined as $SBO = q_w/(Gi_{pc})$, where q_w, G and i_{pc} are heat flux, mass flux, and CO_2 enthalpy at T_{pc}, respectively. SBO, by coupling the density ratio between "liquid" and "vapor", represents the competition between vapor expansion induced momentum force and inertia force. The experiment of supercritical CO_2 heat transfer is performed in a 10.0 mm inner diameter tube, covering ranges of $P = 7.5$–21.1 MPa, $G = 488$–1600 kg/m²s and $q_w = 74$–413 kW/m². Surprisingly, the onset of HTD is found to occur at a critical SBO which is 5.126×10^{-4} and the critical heat flux is expressed as $q_{CHF} = 5.126 \times 10^{-4} Gi_{pc}$. It is shown that our new criterion is also suitable for other experiments reported in literature, providing a general guidance to design and operate S−CO_2 heaters to avoid HTD.

1. Introduction

The supercritical water heat transfer has been widely investigated since 1950s [1,2]. The studies are driven by the development of advanced nuclear reactors using supercritical water as the coolant, which have higher thermal efficiencies due to distinct cycle performance and simplified system layout. For example, the steam separator and dryer are not necessary in such a system [3]. However, the supercritical water-steam power plant also has drawbacks. It is known that the system efficiency is increased by increasing the vapor temperature entering turbine. Such improvement is restricted by the temperature tolerance limit of materials. At ultra-high temperature such as 700 °C, the chemical reaction between water-steam and solid material is enhanced, introducing the difficulty to further explore efficiency potential [4,5].

An alternative fluid is carbon dioxide, having critical parameters of $P_c = 7.38$ MPa and $T_c = 31.05$ °C, which are significantly lower than those of water. CO_2 is easier to reach the supercritical state than water. Besides, CO_2 is more inert than water, offering the possibility using higher vapor parameters to improve the cycle efficiency [6]. Recently,

great attention has been paid to the supercritical CO_2 cycle to convert thermal energy into power using nuclear energy, solar energy or coal as energy resources [7–9]. For these applications, a heater is necessary to receive heat from a heat source. Better understanding of supercritical CO_2 heat transfer is not only useful for the estimation of heat transfer area, but also important for the safety analysis of power plant. The appearance of heat transfer deterioration (HTD) should be avoided. HTD would cause the failure of heater surface [10].

Considering supercritical CO_2 flowing in a heated tube, there are three heat transfer modes: (1) normal heat transfer (NHT): When the bulk fluid temperature is far away from pseudo-critical temperature (T_{pc}), conventional convection heat transfer exists. Heat transfer can be well predicted using the single-phase Dittus-Boelter correlations, or modified correlations [11]. (2) enhanced heat transfer: When the bulk fluid temperature is very close to pseudo-critical temperature, heat transfer may be enhanced [12]. (3) heat transfer deterioration (HTD): When the pseudo-critical temperature T_{pc} is between heater surface temperature $T_{w,in}$ and bulk fluid temperature T_b, $T_{w,in} > T_{pc} > T_b$, heat transfer may be deteriorated to show a sharp rise of heater surface

---

temperatures along flow direction [13]. In this paper, why normal heat transfer is switched to heat transfer deterioration is explained. Thus, normal heat transfer and enhanced heat transfer are combined to the normal heat transfer category.

Our literature survey shows that the investigation of heat transfer deterioration is not sufficient, from both fundamental understating point of view and application point of view. The available studies emphasize the importance of large variation of thermo-physical properties, buoyancy effect and acceleration effect [14–16]. A simple treatment is to plot $q_w \sim G$ curve to distinguish HTD and NHT, where q_w and G are inner wall heat flux and mass flux, respectively. Different authors obtained different curves. For example, Kim et al. [17] presented $q_w = 0.0002G^2$, but Yamagata et al. [18] gave $q_w = 0.2G^{1.2}$. It is noted that the $q_w \sim G$ curves are experimentally correlated, which do not reflect the mechanism of heat transfer deterioration.

Great attention has been paid to analyze the buoyancy effect and acceleration effect on heat transfer. Jackson et al. [19] gave a buoyancy effect parameter, which is written as $Gr/Re^{2.7}$, where Gr and Re are Grashof number and Reynolds number, respectively. They recommended that when $Gr/Re^{2.7} < 10^{-5}$, the buoyancy effect can be ignored, otherwise, it should be considered for vertical flows. Huang et al. [14] listed some criteria to predict the onset of buoyancy influence. They noted discrepancies between correlations and experimental data, and pointed out that new correlations to accurately predict the buoyancy effect are necessary.

Zhang et al. [20] performed S−CO_2 heat transfer in a 16 mm inner diameter tube with the ranges of pressures, mass fluxes and heat fluxes of 7.5–10.5 MPa, 50–500 kg/m^{2}s and 5–100 kW/m^2, respectively. Heat transfer at lower mass flux was not deteriorated but rather enhanced with a rising heat transfer coefficient. Results suggested that the special heat transfer enhancement at lower mass flux was possibly induced by the combined effects of strong buoyancy effect and high specific heat of the fluid. A modified correlation for S−CO_2 heat transfer at low mass flux was proposed. Zhang et al. [21] summarized the existing identification methods for HTD. They found that, the most common identification method cannot reflect the actual location where HTD occurs. The reference value representing normal heat transfer is observed to be important in judging the heat transfer state. An improved identification method of HTD suitable for both supercritical water and supercritical CO_2 is proposed. The new method shows favorable accuracy in discerning HTD and NHT.

Here, a general criterion to predict the onset of HTD for supercritical CO_2 heat transfer is developed. This paper consists of two parts. In the first part, a new theory is established to explain the HTD mechanism. Our theoretical work is based on the pseudo-boiling assumption, which is similar to the post-dryout heat transfer of subcooled boiling at subcritical pressure. A clear physical picture is given, containing a vapor layer on tube wall, beyond which is the "subcooled" liquid in core flow. The two fluid layers are interfaced at the pseudo-critical temperature, which is treated as the "saturation temperature interface". The subcritical boiling number is extended to yield supercritical "boiling" number. For such similarity, fluid enthalpy at the pseudo-critical point is used instead of the latent heat of evaporation at subcritical pressure. Our own experimental data and others in literature support our theoretical analysis. It is found that the onset of HTD exactly occurs at a critical supercritical "boiling" number of 5.126×10^{-4}. Our criterion comprehensively considers effects of heat flux, mass flux and operation pressure. It is concluded that the tube diameter does not influence the onset of HTD, but influences the amplitude of temperature overshoot once HTD occurs.

2. CO₂ physical properties and near-wall velocity distribution

Fig. 1 shows the CO_2 physical properties at three pressures of $P = 8$, 15 and 20 MPa, covering the pressure range in our experiment. The 8 MPa pressure is close to the critical pressure of 7.38 MPa. For pressure
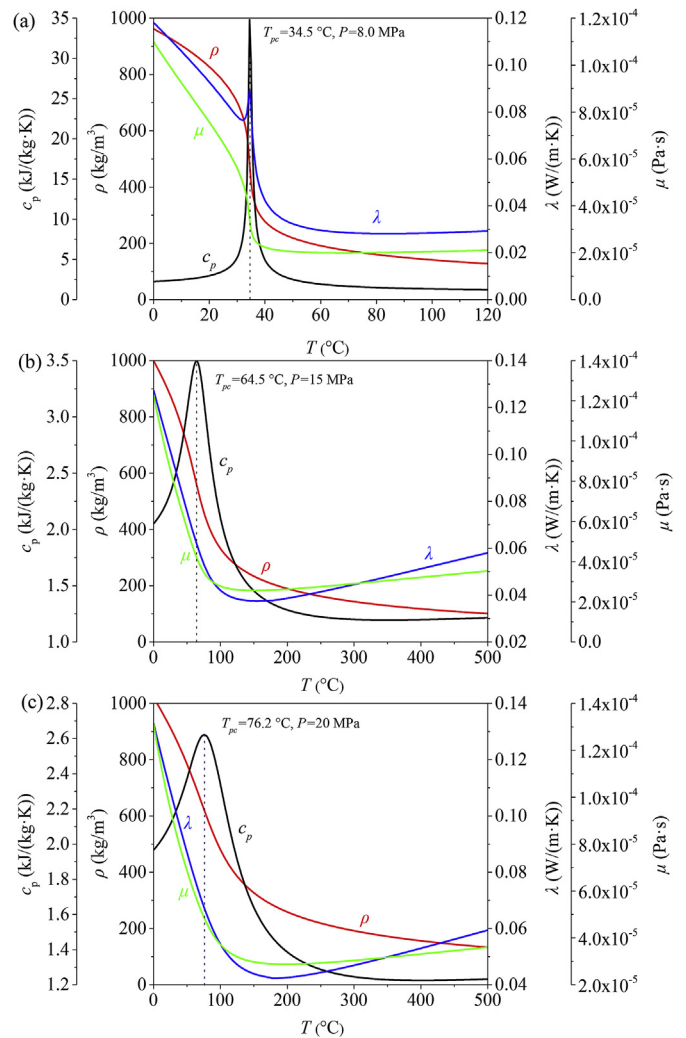

Fig. 1. Thermal-physical properties of supercritical CO_2 at pressures of 8, 15 and 20 MPa.

larger than the critical pressure, the location of peak specific heat is defined as the pseudo-critical point, which shifts to higher temperatures when pressure increases. The pseudo-critical temperatures, T_{pc}, are 34.5 °C, 64.5 °C and 76.2 °C respectively at the three pressures. CO_2 behaves the liquid-like for $T < T_{pc}$ and the vapor-like for $T > T_{pc}$. All the physical properties such as density ρ and thermal conductivity λ are sharply changed near T_{pc}. The pressures apparently influence physical properties, especially near T_{pc}. When pressure increases, the slopes of various parameters versus temperatures become gentler. Later it will be shown that this behavior influences the onset of HTD. The physical properties contain uncertainties at the pseudo-critical temperature because they are very sensitive to the temperature variations near T_{pc}.

To understand the convective CO_2 heat transfer, the axial flow velocity profile is plotted in log-linear coordinates with law-of-wall normalizations near a smooth-flat-plate turbulent boundary layer [22] (see Fig. 2). The flow is divided into an inner layer and an outer layer. The two layers are overlapped by a logarithmic layer. The inner layer contains a viscous sublayer, a buffer layer and a logarithmic layer. In the viscous layer, the transfer of momentum and heat is due to viscous effect. The layer is very thin typically in several microns. The logarithmic layer is dominated by inertia effect, but the buffer layer is affected by both viscous effect and inertia effect. The above discussion is for adiabatic flow. To date it is not clear how the heating condition influences the near-wall flow structure. In this paper, the thickness at the end of buffer layer is assumed as the thermal boundary layer,
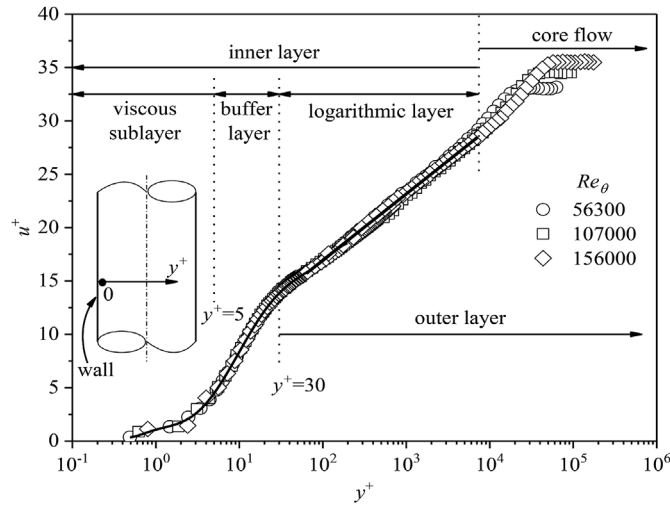
Fig. 2. Non-dimensional axial velocity near the tube wall for turbulent flow (the figure is re-plotted based on ref. [22].).

covering a thickness of $y^+ = 30$, in which y$^+$ and u^+ are defined as

$$y^+ = \frac{u^*y}{\nu} \tag{1}$$

$$u^+ = \frac{u}{u^*} \tag{2}$$

where u^* is the shear velocity, which is $u^* = \sqrt{\tau_w/\rho}$, τ_w is the shear stress at the wall, which is $\tau_w = f\rho_b u_b^2/8$, f is the friction factor: $f = (1.82\log Re_b - 1.64)^{-2}$, y is the distance from the wall, u is the axial velocity and u^+ is the non-dimensional axial velocity.

3. Similarity analysis between subcritical boiling and supercritical "boiling"

Here, the similarity analysis between subcritical boiling and supercritical "boiling" is performed. The subcooled flow boiling is considered first. When the wall heat flux is high and the bulk fluid is subcooled, $T_b < T_{sat}$, where T_b is the bulk liquid temperature and T_{sat} is the saturation temperature at operation pressure, bubbles are nucleated and growing on the wall (see Fig. 3a). These bubbles detach the wall, but are completely condensed by the bulk subcooled liquid, yielding no apparent net vapor generation in the tube core. If the heat flux is sufficiently high, bubbles may not detach the wall. They are merged to form a vapor blanket to trigger the critical heat flux (CHF, see Fig. 3b).

CHF should be avoided to prevent the tube from damage. The onset of vapor blanket formation depends on complicated bubble dynamics and phase change mechanisms, which are beyond the scope of this paper. Here, an important parameter, K_1 number, is paid attention. This parameter was proposed by Kandlikar [23]. Considering a bubble on a tube wall, the evaporation on bubble interface results in an evaporation mass flux of q_w/i_{fg}, where i_{fg} is the latent heat of evaporation, see Fig. 3c. The resulting momentum change results in a force on the vapor-liquid interface that can be expressed as

$$F_{M'} = \left(\frac{q_w}{i_{fg}}\right)^2 \frac{D}{\rho_g} \tag{3}$$

where D is the bubble diameter and ρ_g is the vapor density. Other force acting on the bubble interface includes an inertia force, which is written as

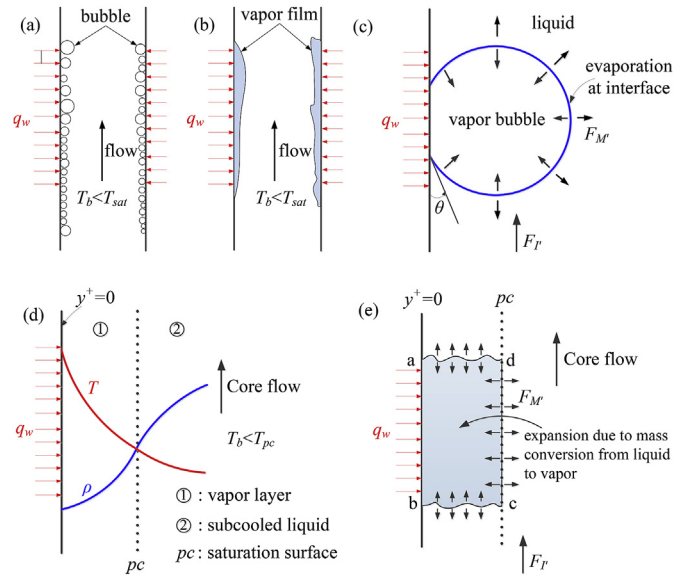$$F_{I'} = \frac{G^2 D}{\rho_f} \tag{4}$$

Fig. 3. Similarities of subcooled boiling at subcritical and supercritical pressures (a: bubbles on the wall for subcritical boiling, b: vapor on the wall for subcritical boiling, c: forces on bubble for subcritical boiling, d: temperatures and densities inside and outside of the "saturation temperature interface" for supercritical "boiling", e: forces on "vapor film" for supercritical "boiling").

where ρ_f is the liquid density. The K_1 number reflects evaporation momentum force relative to inertia force:

$$K_1 = \frac{F_{M'}}{F_{I'}} = \left(\frac{q_w}{Gi_{fg}}\right)^2 \frac{\rho_f}{\rho_g} = \frac{\rho_f}{\rho_g} Bo^2 \tag{5}$$

where Bo is the boiling number, $Bo = q_w/(Gi_{fg})$. For a fixed density ratio when a working fluid is given, the boiling number is useful to characterize the heat transfer mechanism. Previously, the boiling heat transfer in microchannels with a hydraulic diameter of 155.4 μm using acetone as the working medium is reported [24]. It is found that boiling in microchannels displays three distinct regimes. The moderate boiling number range results in nucleate boiling mechanism, with heat transfer coefficients dependent on heat fluxes, not dependent on mass fluxes and vapor mass qualities. The higher boiling number range results in convective mechanism, with heat transfer coefficients dependent on mass fluxes, but not dependent on heat fluxes. The transition between nucleate boiling and convective evaporation reflects the competition between bubble expansion induced momentum force and inertia force on heat transfer.

Now the theoretical analysis at supercritical pressure is dealt with. The phase change (boiling or condensation) does not occur at supercritical pressure. However, the pseudo-boiling concept can still be used. Fig. 3d and e shows a thin boundary layer, having $T_{w,in} > T_{pc} > T_b$. The layer on the wall has low fluid density, which is treated as "vapor" layer. Beyond T_{pc} is the core flow having high fluid density, which is treated as "subcooled" liquid due to $T_b < T_{pc}$. Because at $T = T_{pc}$, the vapor layer expands due to the moving away of T_{pc} line from the wall to result in a vapor mass increment, T_{pc} is regarded as the "saturation temperature". Thus, a vapor expansion induced momentum force exists at the T_{pc} interface. If the inertia force is large enough to suppress the vapor expansion induced momentum force, the vapor layer either becomes thinner, or is broken due to strong subcooled liquid flushing, under which the heater surface is rewetted by subcooled liquid. The decreased vapor layer thickness and/or broken vapor layer improve heat transfer to keep normal heat transfer. On the contrary, if the inertia force is small so that it cannot suppress the vapor expansion induced momentum force, the vapor layer becomes thicker to trigger the onset of HTD. Fundamentally, the mechanism is similar to subcooled

boiling at subcritical pressure.

The near-wall flow structure includes a viscous layer and a buffer layer. The relationship between near-wall flow structure and vapor layer thickness terminated at $T = T_{pc}$ is described here. Considering a supercritical CO_2 flowing in vertical tubes with wall heat flux q_w, there may be one or two peaks of wall temperatures. The first wall temperature peak appears due to low thermal conductivity of vapor layer, followed by a subsequent decrease of wall temperatures due to the temporary increase in shear turbulence production. The second wall temperature peak is due to the decrease of shear turbulence production associated with velocity peak in buffer layer. In other words, the non-dimensional vapor layer thickness $y_{T_{pc}}^+$ is varied along axial flow direction. With flow development from inlet to outlet, the location of $y_{T_{pc}}^+$ continuously moves towards the channel centerline as fluid receives heat flux. During this process, $y_{T_{pc}}^+$ may cross the buffer layer. The two locations of $y^+ = 30$ and $T = T_{pc}$ do not coincide with each other. The relationship between near-wall flow structure and heat transfer deterioration should be investigated in the future.

It is noted that q_w/i_{fg} represents the evaporation mass flux on bubble interface for subcritical boiling. Because there is no "latent heat of evaporation" at supercritical pressure, it is difficult to decide the vapor expansion induced mass increment for the development of supercritical "boiling" number. Due to large density variation across T_{pc}, a small mass increment causes a significantly large volume expansion to induce a momentum force.

Fig. 4 shows T (temperature)$\sim i$ (enthalpy) curves at subcritical pressure and supercritical pressure. When pressure is raised, the latent heat of evaporation is decreased, which is zero at the critical point c. The red curves in Fig. 4 illustrate supercritical pressure cases with the pseudo-critical point marked as pc. At supercritical pressure, the enthalpy cannot be changed at a constant temperature, which is different from subcritical pressure. Thus, a small temperature variance δ deviating from T_{pc} is introduced to characterize the enthalpy change for the vapor expansion induced mass increment:

$$\Delta i = i_{T_{pc}} - i_{T_{pc}-\delta} \tag{6}$$

Because δ is unknown, the following assumption is made

$$\Delta i = i_{T_{pc}} - i_{T_{pc}-\delta} = k \cdot i_{T_{pc}} \tag{7}$$

where k is a constant, $k \ll 1$. Thus, the mass exchange flux across T_{pc} interface is scaled as q_w/i_{pc}, which results in the supercritical "boiling" number as
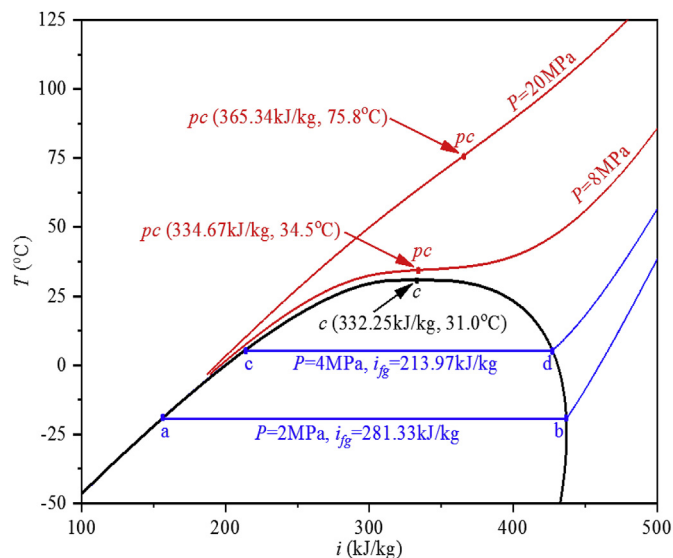

Fig. 4. T-i curves of CO_2 at subcritical pressure and supercritical pressure.
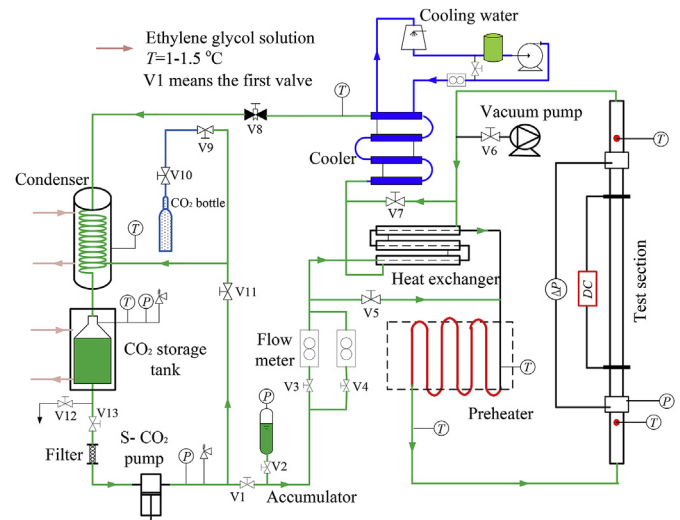

Fig. 5. Experimental setup of present study.

$$SBO = \frac{q_w}{Gi_{pc}} \tag{8}$$

SBO reflects the comprehensive effects of heat flux q_w and mass flux G. The effect of pressure is implicitly included in enthalpy at i_{pc}. Because i_{pc} increases with increase of pressure, the increased pressure decreases vapor mass increment to weaken the vapor expansion induced momentum force. Thus, heat transfer can be improved at higher pressures. A transition boundary of supercritical "boiling" number is expected to distinguish normal heat transfer and heat transfer deterioration, which will be verified by the following experiments.

4. Experimental apparatus and procedure

4.1. Experimental system

Fig. 5 shows the experimental setup. The maximum CO_2 pressure and temperature are 25 MPa and 500 °C, respectively. The experiment loop consists of following parts: a gas-vacuum/CO_2-charging system, a convective CO_2 loop, a cooling water loop, an electric heating system and a data acquisition system. The convective CO_2 loop is a closed system. The CO_2 fluid has a purity of 99.9%. Initially, by switching on V6 and operating a vacuum pump, the convective CO_2 loop is vacuumed to an ultra-low vacuum pressure. Then, by switching on V10, CO_2 is charged into a storage tank from a high-pressure bottle. In order to keep the liquid state of CO_2 in the storage tank, the ~1 °C chiller water is circulated to cool the outer surface of the storage tank. A piston pump sucks the low temperature CO_2 liquid from the CO_2 storage tank. The generated flow rate is divied into two paths. One path is bypassed to the storage tank, and the other path consecutively flows through two parallel mass flow meters, the tube side of a heat exchanger, a preheater and a test tube. The CO_2 vapor at test tube outlet flows through the shell side of the heat exchanger, a cooler and finally returns to a condenser. The recuperator heat exchanger dissipates heat from high temperature CO_2 vapor to cold CO_2 liquid of pump outlet. The heat received from the test tube is dissipated to cooling water, which is circulated by a cooling tower and dissipates heat to environment.

In order to achieve stable pressure during operation, a pressure vessel stabilizer is installed at the pump outlet. The high-pressure nitrogen gas is charged in the stabilizer but it is separated from CO_2 liquid by a flexible membrane. The preheater and test tube are heated by low direct-current (DC) voltage using the resistance heating principle. The heating power can be easily changed by adjusting the DC voltage. The preheater and test tube are heated by two independent power supply systems, having parameters of 54 kW (0–36 V, 0–1400 A), and 120 kW
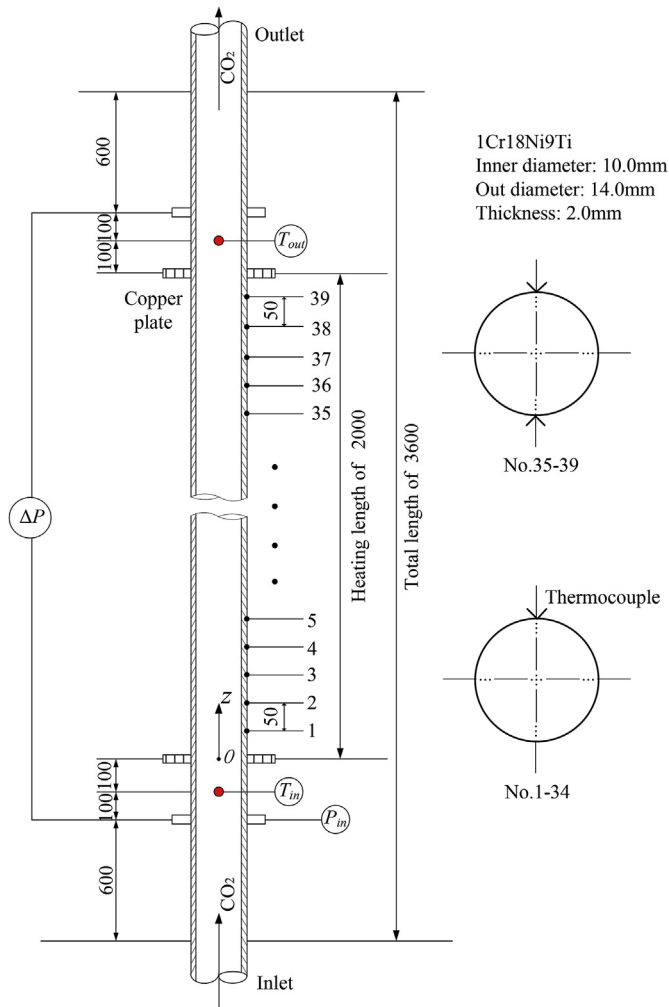
Fig. 6. Test tube.

Table 1
Parameter measurements and uncertainties.

Parameters	Range	Uncertainty
pressure P	7.5–21.1 MPa	0.958%
differential pressure ΔP	5.7–48.5 kPa	2.06%
inlet fluid temperature T_{in}	10–120 °C	0.5 °C
outlet fluid temperature T_{out}	25–200 °C	0.5 °C
outer wall temperature $T_{w,out}$	34–468 °C	0.5 °C
mass flux G	488–1600 kg/m²s	2.05%
heating power Q	4.65–25.9 kW	3.25%
heat flux q_w	74–413 kW/m²	5.05%
Heat transfer coefficient h	0.786–10.6 kW/m²K	5.66%

$(0-40\,\mathrm{V},\ 0-3000\mathrm{A})$, respectively. The heated tube is electrically insulated from other part of the loop component.

4.2. Test tube

The test tube has vertically upward flow, which is made of 1Cr18Ni9Ti with an outer diameter 14.0 mm and an inner diameter 10.0 mm (see Fig. 6). The tube is 3600 mm in length with an effective heating length of 2000 mm. Two stabilization sections, one before entering the heating section, and the other beyond the heating section, are arranged, each having a length of 800 mm. The DC power is applied via two copper electrodes, which are welded with the tube. The thermocouple wires are welded on outer tube surface by a specifically designed
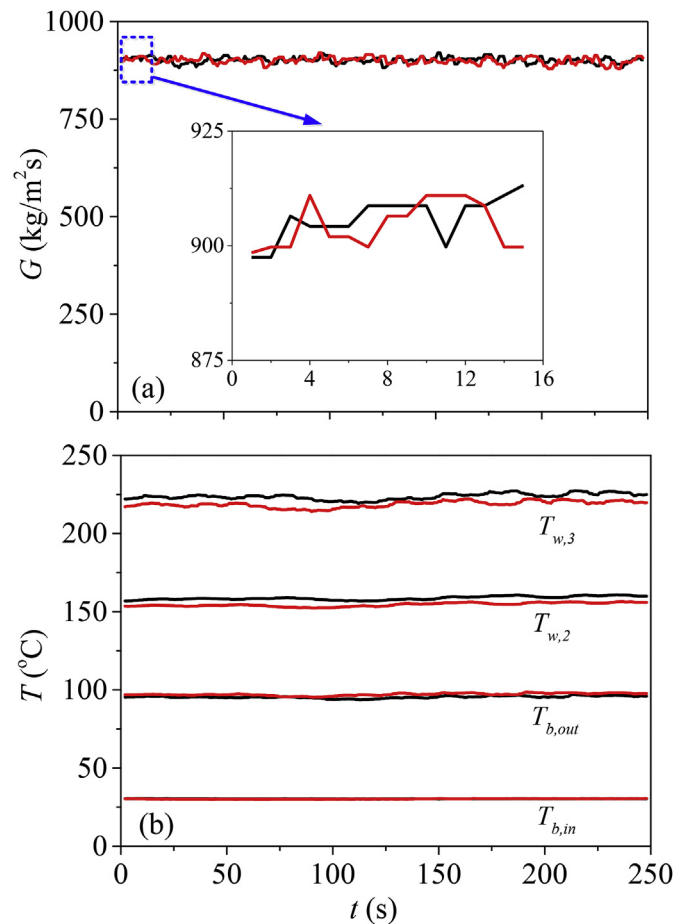

Fig. 7. Repeatable and stable measurements (black curves for 7.585 MPa, 892.5 kg/m²s and 255.98 Kw/m², red curves for 7.579 MPa, 896.8 kg/m²s and 254.6 Kw/m², both with time sampling rate of 1s).

capacitance impact welding machine, ensuring no thermal resistance between thermocouples and tube wall. These thermocouples are arranged on 39 cross-sections along flow direction. The axial distance between two neighboring cross-sections is 50 mm. Some cross-sections have just a single thermocouple, but some cross-sections have two thermocouples. Due to the geometry symmetry, the two readings of thermocouples on a specific cross-section are almost identical. The test tube is wrapped by a 50 mm thickness thermal insulation material, having thermal conductivity as low as 0.036 W/mK to keep high thermal efficiency of the test tube.

4.3. Date reduction

The measurements include inlet pressure P_{in}, pressure drop ΔP, inlet fluid temperature T_{in}, outlet fluid temperature T_{out}, various thermocouples welded on outer wall surface, and CO_2 flow rate m. The calibration experiment is performed to determine the thermal efficiency of test tube:

$$\eta = \frac{m \cdot (i_{out} - i_{in})}{U \cdot I} \tag{9}$$

where i_{out} and i_{in} are the outlet and inlet enthalpies determined by their corresponding pressure and temperature, respectively, U and I are voltage and current applied to the test tube. The mass flux G is

$$G = m / \left(\frac{1}{4} \pi d_{in}^2 \right) \tag{10}$$

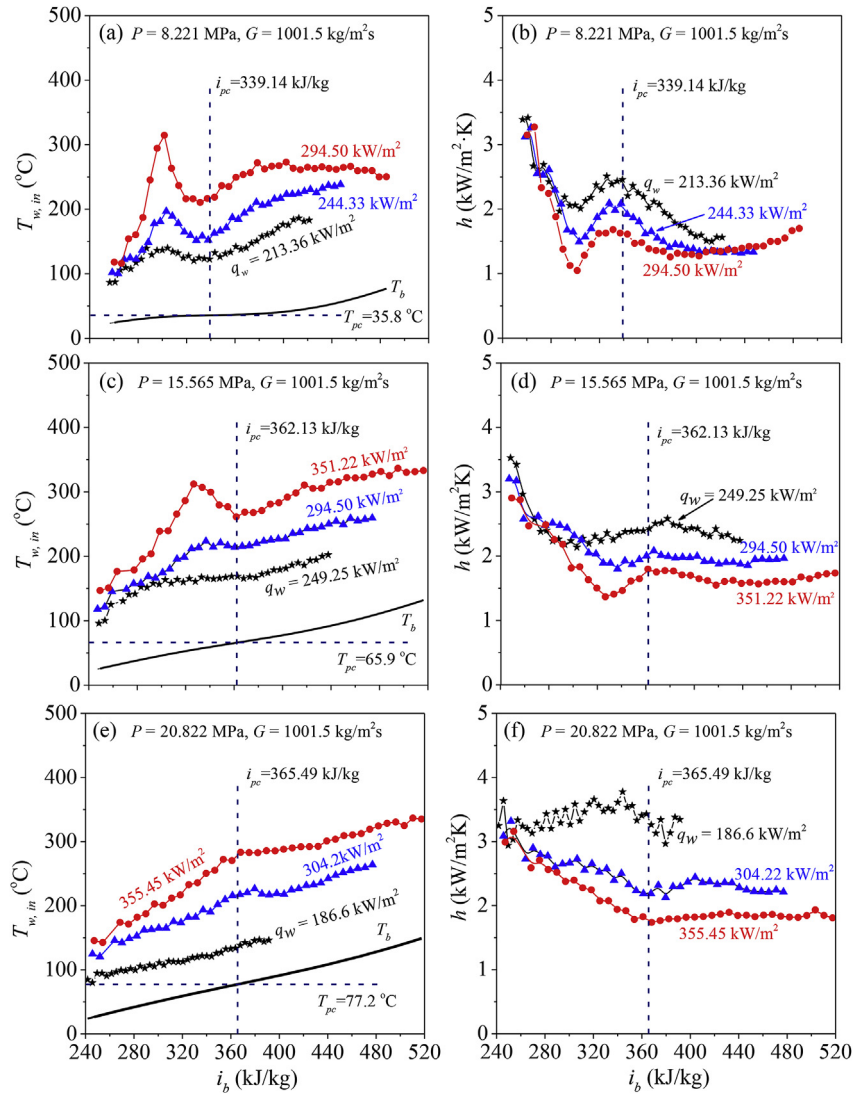where d_{in} is the inner diameter of test tube ($d_{in} = 10.0$ mm here). Our

Fig. 8. Effect of heat fluxes on inner wall temperatures and heat transfer coefficients (present data).

calibration experiment indicates thermal efficiencies of about 91% for most of runs, indicating high performance of our supercritical pressure heat transfer facility. For our data reduction, the heating power of $Q = m(i_{out} - i_{in})$ is directly used. The heat flux based on inner tube wall surface area is

$$q_w = \frac{Q}{\pi d_{in} L} = \frac{m(i_{out} - i_{in})}{\pi d_{in} L} \tag{11}$$

where L is the effective heating length, $L = 2000$ mm here. The heat transfer coefficients h are obtained along the axial flow length:

$$h = \frac{q_w}{T_{w,in} - T_b} \tag{12}$$

where $T_{w,in}$ is the inner wall temperature and T_b is the bulk fluid temperature, which are dependent on axial flow length. T_b is decided based on running pressure P and local enthalpy i_b, which is based on energy conservation equation:

$$i_b = i_{b,in} + \frac{q_w \pi d_{in} z}{m} \tag{13}$$

where $i_{b,in}$ is the enthalpy based on pressure P and inlet fluid temperature T_{in}, and z is the axial length starting from the heating electrode (see Fig. 6).

Due to the vertical upflow and uniform heating on the tube wall

surface, the inner wall temperature $T_{w,in}$ can be predicted using the one-dimension thermal conduction equation:

$$\frac{1}{r}\frac{d}{dr}\left(r\lambda\frac{dT}{dr}\right) + q_v = 0 \tag{14}$$

where λ is the thermal conductivity of tube. Equation (14) satisfies following boundary conditions:

$$\left.\frac{dT}{dr}\right|_{r=r_{oou}} = 0 \tag{15}$$

$$T|_{r=r_{out}} = T_{w,out} \tag{16}$$

where r_{out} is the outer tube radius and $T_{w,out}$ is the outer wall temperature measured by thermocouple. In Eq. (14), q_v is the heat generation rate per unit volume due to resistance heating:

$$q_v = \frac{Q}{\pi(r_{out}^2 - r_{in}^2)L} \tag{17}$$

Equation (14), subjecting to the boundary conditions Eqs.(15) and (16), yields $T_{w,in}$ as

$$T_{w,in} = T_{w,out} - \frac{q_w r_{in}}{2\lambda}\left(\frac{a^2 - 2\ln a - 1}{1 - a^2}\right) \tag{18}$$

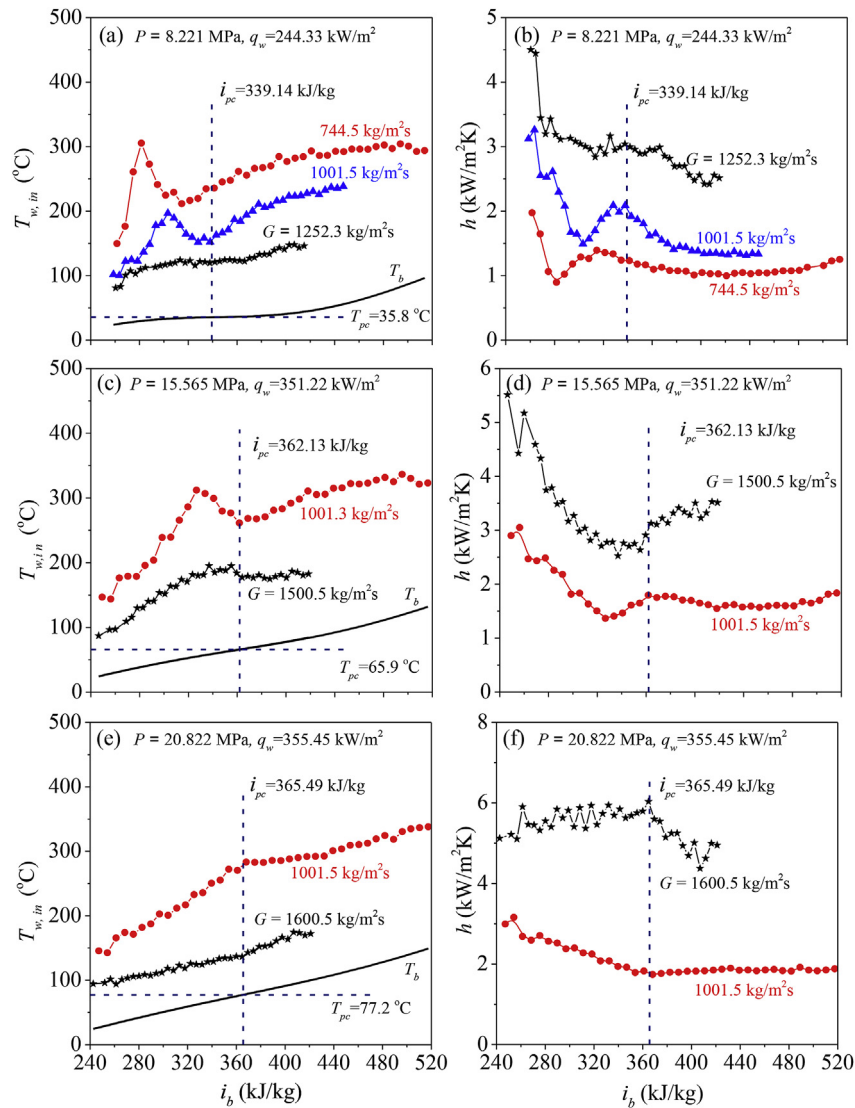where a is the ratio of inner tube radius to outer tube radius: $a = r_{in}/$

Fig. 9. Effect of mass fluxes on inner wall temperatures and heat transfer coefficients (present data).

r_{out}.

4.4. Parameter uncertainties

Table 1 lists the measurement and calculated parameters. The mass flow rate is measured by one of the two Coriolis mass flow meters, DMF-1-3-B with a mass flow rate range of 0–1000 kg/h and DMF-1-2-A with a mass flow rate range of 0–200 kg/h, both having accuracies of 0.2%. Based on required mass flow rate, one of the two mass flow maters is selected by switching on one of the two valves with the other valve off. The fluid temperatures are measured by K-type jacket thermocouples with diameter of 2.0 mm. The wall temperatures are measured by wall-welded thermocouple wires with diameter of 0.25 mm. These thermocouples have accuracies of 0.5 °C after calibration. The fluid pressure is measured by Rosemount 3051 pressure transducer with an accuracy of 0.1%. The pressure drop is measured by Rosemount 1151 differential pressure transducer with an accuracy of 0.05%. The pressure or differential pressure transducers sustain high pressures such as 30 MPa. To determine heating power applied to the test tube, the DC (direct-current) voltage and current come from the readings of a voltage converter (0 − 5 V range) and a current converter (0–75 mV), respectively. The real voltage and current applied to the test tube are linearly related to the two readings of the converters with two specific coefficients. All signals are collected by a data acquisition system (ADAM-4118/4117) with an accuracy of 0.2%. The errors of heating power, heat flux and heat transfer coefficient are obtained using the error transmission principle. If a parameter R is related to several independent variables of $x_1, x_2 \ldots x_N$, the error transmission principle gives the uncertainty of R as

$$\Delta R = \sqrt{\left(\frac{\partial R}{\partial x_1}\delta x_1\right)^2 + \left(\frac{\partial R}{\partial x_2}\delta x_2\right)^2 + \cdots\left(\frac{\partial R}{\partial x_N}\delta x_N\right)^2} \tag{19}$$

where $\delta x_1, \delta x_2 \ldots \delta x_N$ are uncertainties of $x_1, x_2 \ldots x_N$. The above process gives uncertainties of 5.05% for q_w and 5.66% for h (see Table 1).

The repeatable experiment is performed before formal experiment. Fig. 7 shows that indeed, the experiment can be repeated for similar running parameters of pressures, mass fluxes and heat fluxes. The red and black curves are performed in the first day and the second day, respectively. Data collected in two different days are almost identical.

5. Results and discussion

Even though the S−CO_2 heat transfer has been investigated for many years, the experiment data are not sufficient to develop a reliable criterion to predict HTD. Most of experiment are performed in near
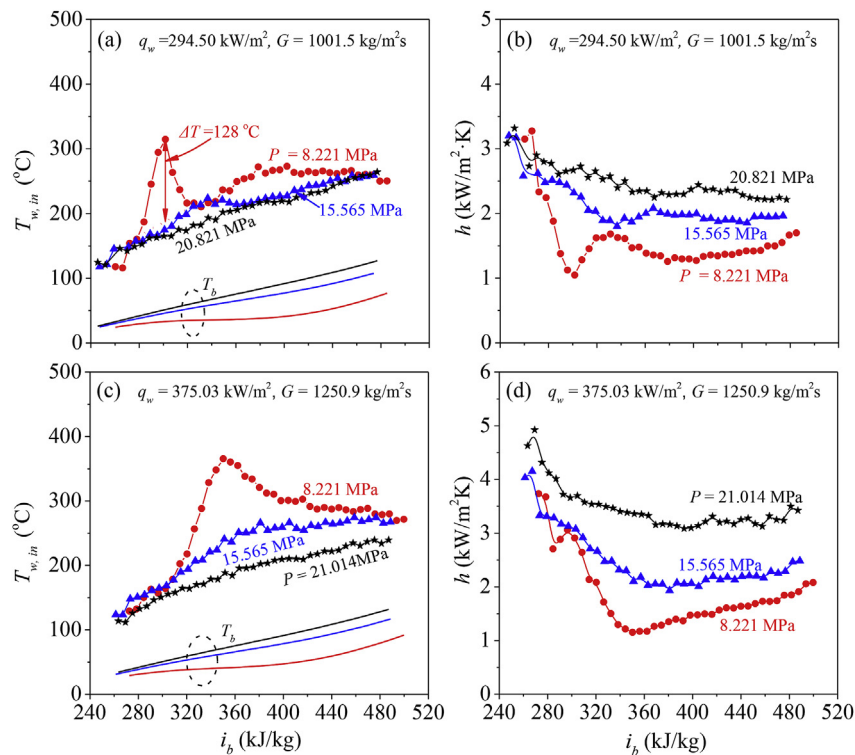
Fig. 10. Effect of pressures on inner wall temperatures and heat transfer coefficients (present data).

critical pressure region of ~ 8 MPa [25,26]. The heat fluxes covered the range of 6–234 kW/m^2 [25]. For practical S−CO$_2$ power plant, the maximum pressures can be several times of critical pressure [27]. The heat flux on heater surface is larger than ~ 100 kW/m^2 [28]. In present experiment, P, G and q_w covered wide ranges having 7.5–21.1 MPa, 488–1600 kg/m^{2}s and 74–413 kW/m^2, respectively, see Table 1. The effects of various parameters on heat transfer are demonstrated first. Then, these data are used to develop a reliable criterion to predict the transition from NHT to HTD.

5.1. Effect of various parameters on S−CO$_2$ heat transfer

Figs. 8–11 demonstrate the effects of heat fluxes, mass fluxes, pressures and tube diameters on wall temperatures and heat transfer coefficients. The left and right columns are wall temperatures $T_{w,in}$ and heat transfer coefficients h, which are presented versus bulk fluid enthalpies i_b. In each figure, the fluid enthalpy at pseudo-critical point, i_{pc}, is marked.

Fig. 8 deals with the effect of heat fluxes. With increase of heat fluxes, wall temperatures are increased, and heat transfer coefficients are decreased. With increase of bulk fluid enthalpies, wall temperatures are either gently increased, belonging to normal heat transfer NHT, or a temperature overshoot appears deviating from NHT, belonging to heat transfer deterioration HTD. The temperature overshoot generally appears ahead of the pseudo-critical point. The heat transfer coefficients reach minimum value at the location of wall temperature overshoot. For pressure near the critical pressure such as P = 8.22 MPa, maximum heat transfer coefficients occur near the pseudo-critical point i_{pc}, which is similar to previous studies [29–31]. When pressures are increased to 20.822 MPa, the wall temperature overshoot ahead of pseudo-critical point does not occur (see Fig. 8e).

The effect of mass fluxes G on $T_{w,in}$ and h is opposite to the effect of heat fluxes q_w (see Fig. 9). Larger G improves heat transfer. The effects of heat fluxes and mass fluxes on heat transfer can be explained by the supercritical "boiling" number SBO (see Eq. (8)). The heat flux q_w directly influences the vapor expansion induced mass increment. The

increase in q_w enhances the mass transfer across T_{pc} line, yielding larger vapor expansion induced momentum force to weaken heat transfer. On the other hand, the increase in mass flux G directly enhances the inertia force to improve heat transfer.

Fig. 10 summaries the effect of pressures on heat transfer. As noted already, most of studies reported in literature focus on S−CO$_2$ heat transfer near 8 MPa [25]. Our experiment work extends the pressure range up to ~ 22 MPa, which is ~ 3 times of the CO$_2$ critical pressure 7.38 MPa. The higher pressure operation not only improves heat transfer, but also is useful to eliminate heat transfer deterioration. For example, at q_w = 294.5 kW/m^2 and G = 1001.5 kg/m^{2}s, the pressure P = 8.221 MPa gives a very large temperature overshoot of 128 °C, but the pressure P = 20.821 MPa thoroughly eliminates temperature overshoot (see Fig. 10a). Correspondingly, the 8.221 MPa pressure holds a minimum heat transfer coefficient of 1.047 kW/m^{2}K, but the 20.821 MPa pressure gives heat transfer coefficients above 2 kW/m^{2}K in Fig. 10b.

The supercritical "boiling" number SBO explains the effect of pressures on heat transfer. In section 3, it is indicated that q_w/i_{pc} scales the vapor expansion induced mass increment. Higher pressure elevates i_{pc}, decreasing the vapor expansion induced mass increment to account for heat transfer enhancement. Our finding regarding the effect of pressures on heat transfer provides an important guidance for S−CO$_2$ power plant operation.

Yildiz and Groeneveld [10] assessed the effect of tube diameters on heat transfer. The tube diameters covered a range of 3.18–38.1 mm. They indicated that in normal heat transfer regime, for identical flow conditions, the heat transfer coefficients increase with a decrease in tube diameters. In heat transfer deterioration regime, the heat transfer coefficients also decrease with an increase in tube diameters. They attributed this finding to the increased velocity gradient in radial direction when tube diameter is decreased. Fig. 11 shows the effect of tube diameters on wall temperatures and heat transfer coefficients. The red curves are our own experiment data with inner diameter of 10.0 mm, and the black curves are for tube diameters of 4.5 mm and 8.0 mm coming from Refs. [32,33]. The curves are compared with similar
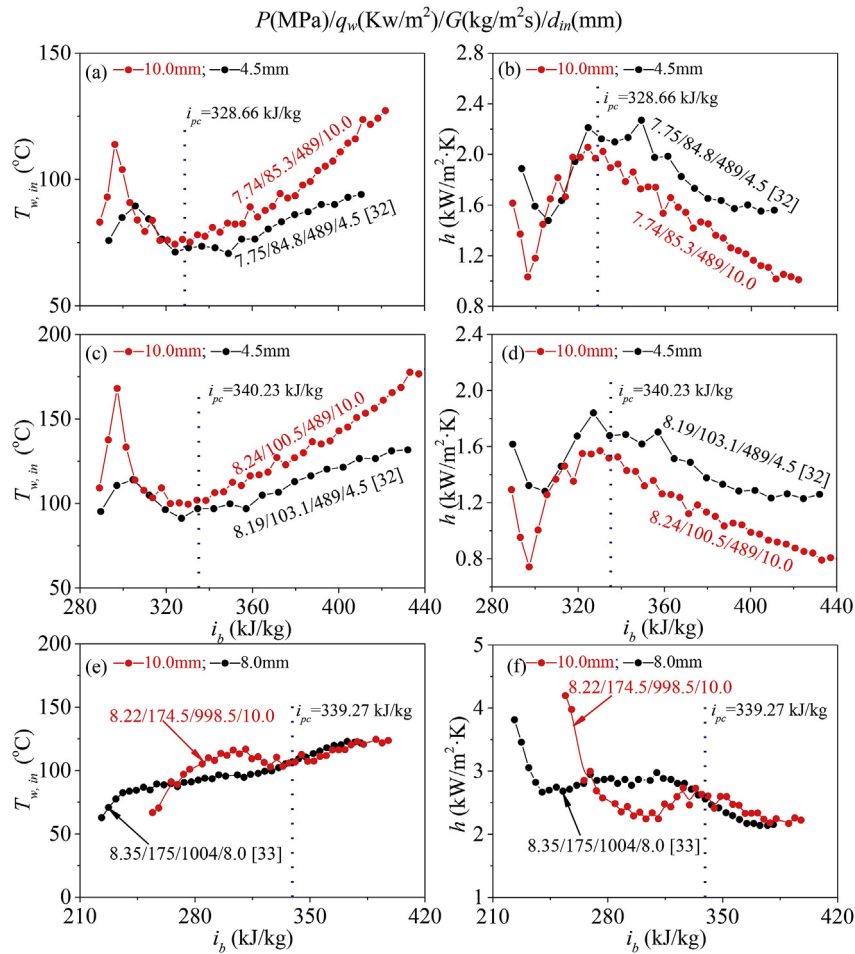
$P(MPa)/q_w(Kw/m^2)/G(kg/m^2 s)/d_{in}(mm)$

Fig. 11. Effect of inner tube diameters d_{in} on wall temperatures $T_{w,in}$ and heat transfer coefficients h (red curves are our present data, and black curves are for data cited from references).

conditions of pressures, heat fluxes and mass fluxes. The comparison outcome is generally consistent with that of ref. [31,34]. The smaller tube diameters result in lower wall temperatures and higher heat transfer coefficients. Besides, it is found that the tube diameters do not influence the transition between normal heat transfer NHT and heat transfer deterioration HTD, but influence the amplitudes of heat transfer coefficients. Even though at a specific mass flux, the decreased tube diameter increases velocity gradient near tube wall to enhance the inertia force applied on the vapor layer, the inertia force characterized by mass flux G is sufficient to distinguish the two regimes of heat transfer.

5.2. The transition boundary from NHT to HTD

The method of judging the occurrence of HTD is presented first. The comparative cases are demonstrated in Fig. 12a and b. For a pair of cases, pressures and mass fluxes are the same, but heat fluxes are different (see Fig. 12a and b). The line connecting points a and b is assumed as the normal heat transfer roadmap. In fact, the wall temperatures may have a temperature overshoot along flow direction, deviating from the assumed roadmap ab. The temperature difference between the maximum temperature and the temperature on the roadmap ab is the temperature overshoot ΔT. In this paper, the criterion of $\Delta T = 8\,°C$ is used to judge the occurrence of heat transfer deterioration, below which normal heat transfer occurs, and above which heat transfer deterioration occurs. Based on this definition, the red curve and black curve belong to heat transfer deterioration HTD and normal heat transfer NHT, respectively (see Fig. 12a and b). For

most of NHT cases, the temperature overshoot is apparently smaller than $8\,°C$. The control of ΔT is important to ensure heater surface safety. If a temperature overshoot exceeds the tolerance of material temperature, the heater transfer tube will be damaged.

Fig. 12c plots the experiment data using vertical coordinate q_w and horizontal coordinate Gi_{pc}. The red and black data points are for HTD with $\Delta T > 8\,°C$ and NHT with $\Delta T < 8\,°C$, respectively. NHT (black color) and HTD (red color) regimes are interfaced by a line. The data are re-plotted using vertical coordinate q_w and horizontal coordinate SBO (supercritical "boiling" number, see Fig. 12d). Surprisingly, the onset of heat transfer deterioration is found to occur at $SBO = 5.126 \times 10^{-4}$, below which normal heat transfer occurs, and beyond which heat transfer deterioration takes place. The transition between the two heat transfer regimes is sensitive to SBO variance. A very small deviation from critical SBO yields the transition from one regime to the other regime. Totally 101 data points are used, including 79 data points having $d_{in} = 10.0\,mm$ for our present data, 2 data points having $d_{in} = 2.0\,mm$ from Ref. [35], 3 data points having $d_{in} = 4.5\,mm$ from Ref. [32], 6 data points having $d_{in} = 6.32\,mm$ from Ref. [31], 7 data points having $d_{in} = 8.0\,mm$ from Ref. [33], and 4 data points having $d_{in} = 10.0\,mm$ from Ref. [16]. Fig. 12 told us that the onset of HTD does not depend on heat flux q_w alone. A specific q_w either behaves normal heat transfer, or behaves heat transfer deterioration, but the onset of HTD depends on the supercritical "boiling" number solely.

The sensitivity of supercritical "boiling" number SBO on the transition from NHT to HTD is examined. Noting the critical value of $SBO_{cr} = 5.126 \times 10^{-4}$, a small variance ahead of SBO_{cr} results in normal heat transfer (see left column of Fig. 13), but a very small variance
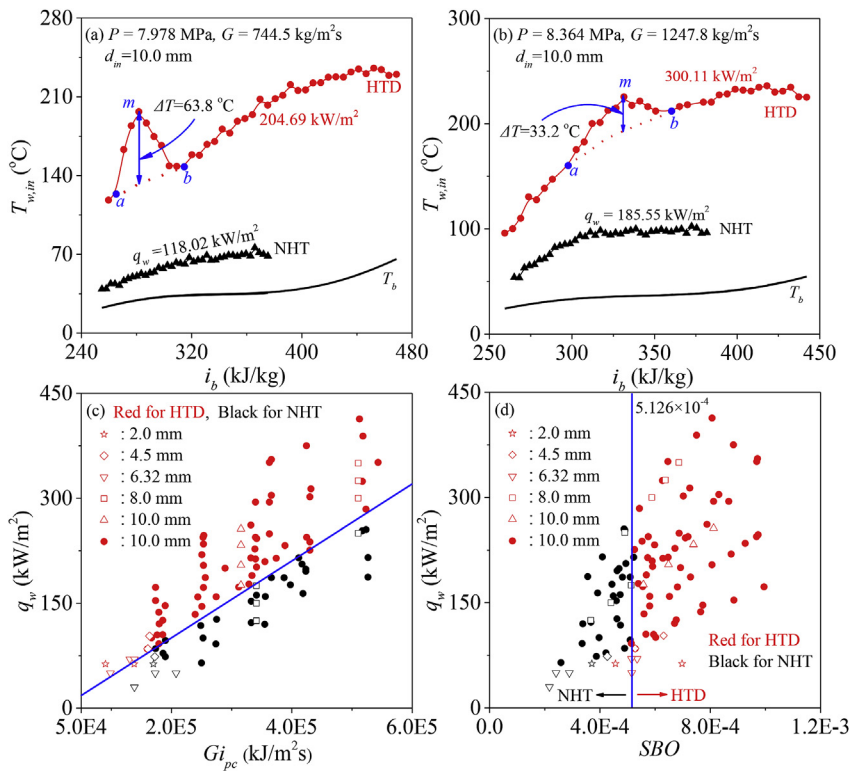
Fig. 12. Normal heat transfer NHT regime and heat transfer deterioration HTD regime (black for NHT and red for HTD, solid symbols for our present data and open symbols for data from references, ◇ & ◇: 7.532–7.745 MPa, 73.5–103.1 kW/m², 488–492 kg/m²s and 4.5 mm in Ref. [32]; ▽ & ▽: 7.75–8.12 MPa, 30–70 kW/m², 285–600 kg/m²s and 6.32 mm in Ref. [31]; △ & △: 7.61 MPa, 175.9–256.2 kW/m², 901.8 kg/m²s and 10.0 mm in Ref. [16]; ☆ & ☆: 7.6 MPa, 63 kW/m², 390–480 kg/m²s and 2.0 mm in Ref. [35]; □ & □: 8.35 MPa, 125–350 kW/m², 1004–1502 kg/m²s and 8.0 mm in Ref. [33]).
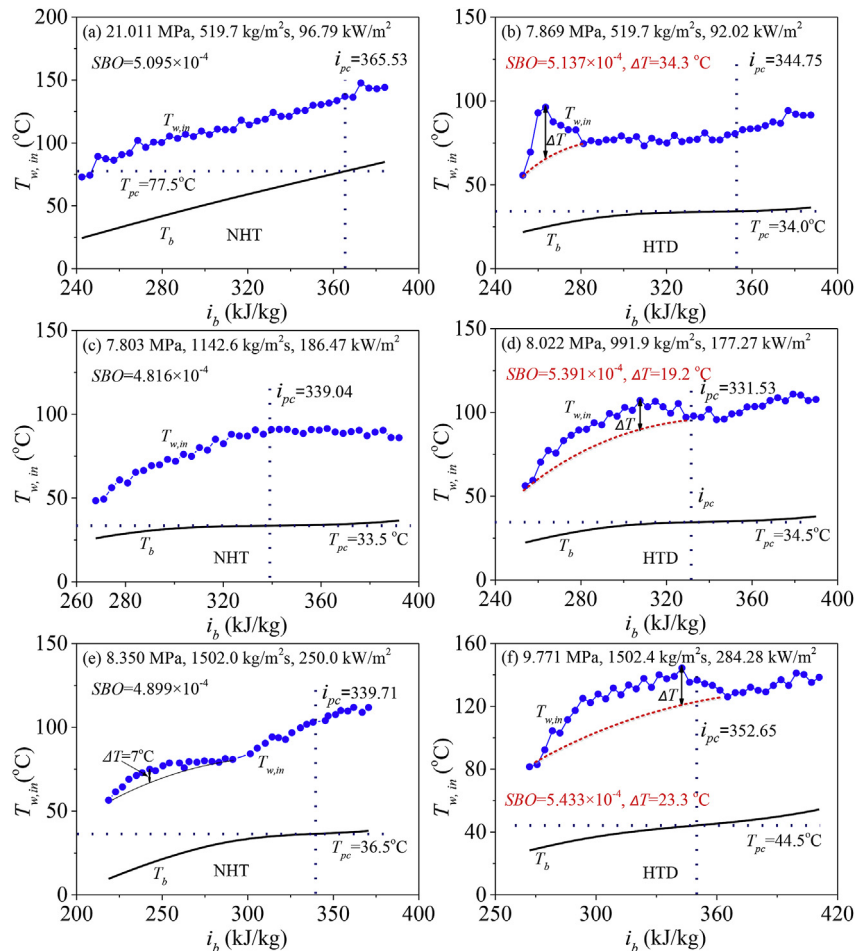

Fig. 13. Very small deviation from critical supercritical "boiling" number causes the transition between NHT and HTD (present data).
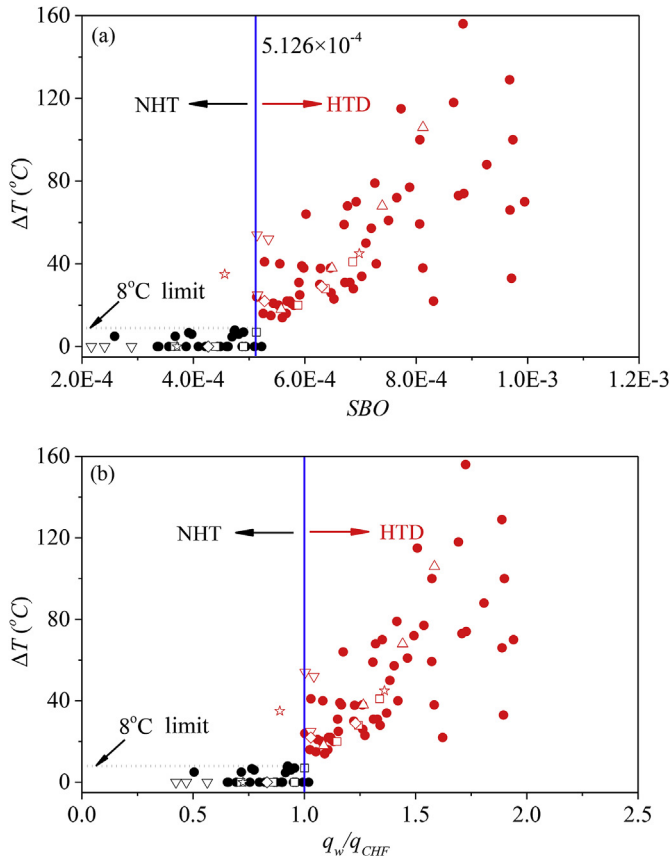
Fig. 14. Transition of heat transfer regimes between NHT and HTD based on SBO and q_w/q_{CHF} (data correspond to Fig.12).

beyond SBO_{cr} results in heat transfer deterioration (see right column of Fig. 13). The transition from NHT to HTD takes place exactly at the critical value without a transition band. The critical value exactly equals to 5.126×10^{-4} for all the experimental data in this paper. It is noted that the running parameters of pressures, heat fluxes and mass fluxes are different from case to case. Physically, the critical SBO value, by coupling the density ratio between "liquid" and "vapor", represents the competition between vapor expansion induced momentum force and inertia force. Below the critical value, the vapor expansion effect is smaller compared to the inertia effect to keep thin vapor layer thickness, maintaining normal heat transfer. Above the critical value, the vapor expansion effect is stronger compared to the inertia effect to expand the valor layer thickness, yielding heat transfer deterioration.

The two regimes of heat transfer are illustrated with vertical coordinate ΔT and horizontal coordinate SBO (see Fig. 14a), using the same data of Fig. 12c and d. It is seen that the temperature overshoot is negligible when $SBO < 5.126 \times 10^{-4}$, but it is obvious when $SBO > 5.126 \times 10^{-4}$. In our experiment, the maximum temperature overshoot is 156 °C occurring at $P = 8.22$ MPa, $G = 1250$ kg/m^{2}s and $q_w = 375$ kW/m^2. The term "critical heat flux (CHF)" for subcritical boiling is introduced to quantify supercritical heat transfer. CHF takes place at the onset of HTD. The corresponding expression yields

$$q_{CHF} = 5.126 \times 10^{-4}Gi_{pc} \tag{20}$$

Because the critical value of 5.126×10^{-4} is determined based on a large quantity of database, Eq. (20) is reliable to predict CHF, covering following data ranges: P in the range of 7.5–21.1 MPa, G in the range of 488–1600 kg/m^{2}s and d_{in} in the range of 2.0–10.0 mm. The prediction capability of CHF beyond the above data ranges are expected to be verified by adding more data. Critical heat fluxes are linearly related to mass flux G and CO$_2$ enthalpy at pseudo-critical point i_{pc}. The high
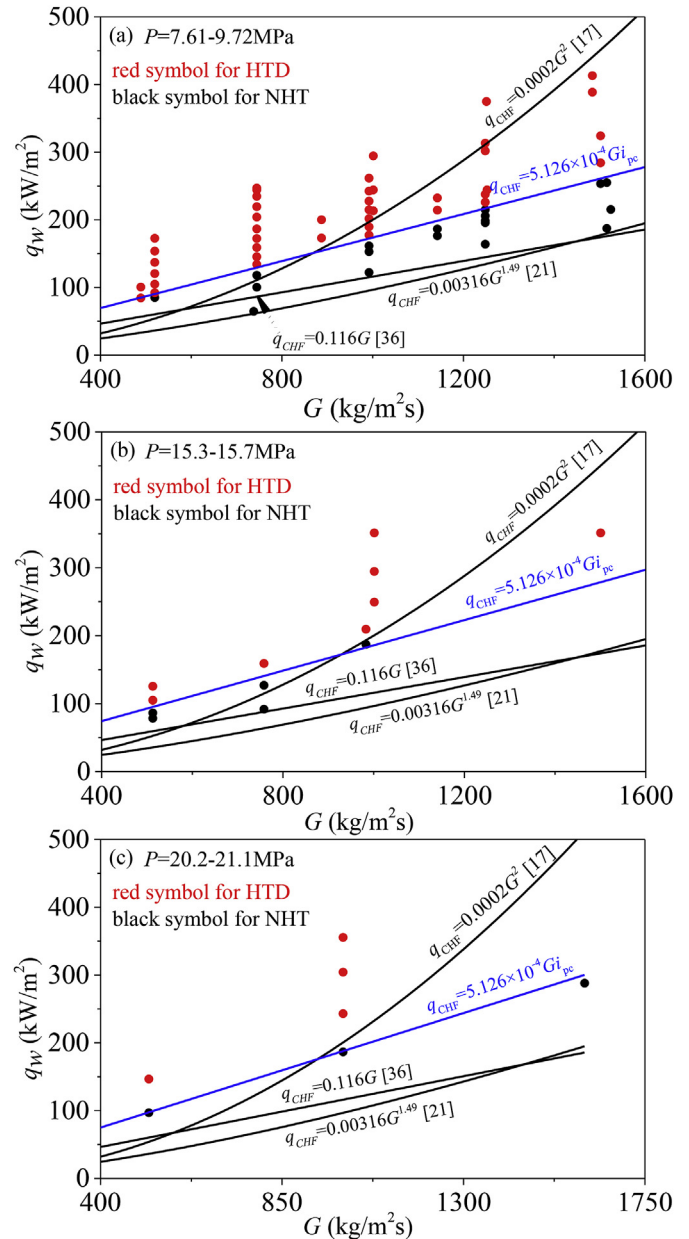

Fig. 15. Identification of the transition boundary from NHT to HTD with a comparison between present experiment data, present correlation and other correlations in the literature.

pressure operation increases i_{pc} to increase CHF, accounting for heat transfer enhancement by increasing pressures. Fig. 14b plots the wall temperature overshoot versus q_w/q_{CHF}.

The transition boundary from NHT to HTD with a comparison between present experimental data, present correlation and other correlations in literature is shown in Fig. 15, using q_w and G as the coordinates. The three subfigures contain three pressure levels, each having a narrow pressure variation. Because our criterion shown in Eq. (20) depends on pressures, the present correlation uses i_{pc} determined at the average pressure in each subfigure. Our correlation well predicts our experimental data for all the three pressure levels. The other three correlations in Refs. [17,21,36] do not consider the effect of pressures. They cannot reflect the correct trend of the transition boundary from NHT to HTD. The correlation of $q_{CHF} = 0.0002G^2$ in Ref. [17] is intercrossed with our prediction curve. The transition boundary curves based on the other two correlations in Refs. [21,36] are under our correlation prediction, indicating that the two correlations overestimate

the heat transfer deterioration regimes. The correlations in the literature are based on the near critical pressure $\sim 8\,\mathrm{MPa}$. Higher pressure data than 8 MPa are very scarce.

Our work starts from the similarity analysis of subcooled boiling at subcritical pressure. In the physical model shown in Fig. 3, the heat transfer deterioration involves a wall-attached vapor layer and a subcooled liquid in core flow. For S−CO_2 heat transfer, indeed, the wall temperature overshoot occurs at the location having the bulk fluid enthalpy apparently smaller than the pseudo-critical enthalpy i_{pc}. Under such circumstance, there is a "saturation temperature" interface located at T_{pc} over the tube cross section. Downstream of the temperature overshoot location, the bulk fluid temperature is increased to make the "saturation temperature" interface vague, recovering the heat transfer performance beyond HTD. When the bulk fluid temperature is beyond the pseud-critical temperature, the variation of physical properties become weak. Thus, heat transfer can be predicted using the well-known turbulent flow and heat transfer theory.

6. Conclusions

To develop a supercritical CO_2 power generation system, it is necessary to develop a critical criterion to judge the onset of heat transfer deterioration. Current theoretical work and experimental data are not sufficient to develop such a criterion. In this paper, the similarity analysis of subcooled boiling at subcritical pressure and supercritical CO_2 heat transfer is performed.

For subcritical boiling, the physical model involves wall attached bubbles and a subcooled liquid core beyond the bubble interfaces. The subcritical boiling number, by coupling the density ratio between liquid and vapor, represents the competition between bubble expansion induced momentum force and inertia force. Larger boiling number may cause coalescence of bubbles to form a vapor blanket. For supercritical heat transfer, the model assumes a "vapor layer" with temperature larger than T_{pc} and a "subcooled liquid" core with temperature smaller than T_{pc}. The subcooled boiling number is extended to supercritical "boiling" number, which is quantified as $SBO = q_w/(Gi_{pc})$. Larger SBO expands "vapor layer" thickness to trigger the HTD.

Experiments are performed with $d_{in} = 10.0\,\mathrm{mm}$, covering the ranges of pressures 7.5–21.1 MPa, mass fluxes 488–1600 kg/m^{2}s and heat fluxes 74–413 kW/m^2. Our own experimental data, incorporating other experiment data of $d_{in} = 2.0$–10.0 mm in references, are used to develop critical SBO, which equals to 5.126×10^{-4}. The temperature overshoot is defined as peak wall temperature deviating from assumed normal heat transfer roadmap. A very small variance larger than critical SBO yields a sharp rise of wall temperatures ahead of pseudo-critical point, followed by heat transfer recovery. Covering our data range, the maximum temperature overshoot reaches up to 156 °C. The SBO comprehensively reflects the effects of heat fluxes, mass fluxes and pressures. It seems that the tube diameters influence the amplitudes of heat transfer coefficients, but do not influence the transition between normal heat transfer and heat transfer deterioration. The developed criterion supports the similarity analysis by assuming pseudo-boiling.

Acknowledgements

Appendix A. Supplementary data

Supplementary data to this article can be found online at https://doi.org/10.1016/j.ijthermalsci.2018.10.032.

References

[1] I.L. Pioro, R.B. Duffey, Experimental heat transfer in supercritical water flowing inside channels, Nucl. Eng. Des. 235 (2005) 2407–2430.

[2] I.L. Pioro, H.F. Khartabil, R.B. Duffey, Heat transfer to supercritical fluids flowing in channels − empirical correlations, Nucl. Eng. Des. 230 (2004) 69–91.

[3] G. Tsiklauri, R. Talbert, B. Schmitt, G. Filippov, R. Bogoyavlensky, E. Grishanin, Supercritical steam cycle for nuclear power plant, Nucl. Eng. Des. 235 (2005) 1651–1664.

[4] C.A. Powell, B.D. Morreale, Materials challenges in advanced coal conversion technologies, MRS Bull. 33 (4) (2008) 309–315.

[5] S.J. Zinkle, G.S. Was, Materials challenges in nuclear energy, Acta Mater. 61 (2013) 735–758.

[6] G.R. Holcomba, C. Carney, Ö.N. Doğan, Oxidation of alloys for energy applications in supercritical CO_2 and H_2O, Corrosion Sci. 109 (2016) 22–35.

[7] J. Sarkar, S. Bhattacharyya, Optimization of recompression S-CO2 power cycle with reheating, Energy Convers. Manag. 50 (2009) 1939–1945.

[8] J. Muñoz-Antón, C. Rubbia, A. Rovira, J.M. Martínez-Val, Performance study of solar power plants with CO_2 as working fluid. A promising design window, Energy Convers. Manag. 92 (2015) 36–46.

[9] Y.L. Moullec, Conceptual study of a high efficiency coal-fired power plant with CO_2 captures using a supercritical CO_2 Brayton cycle, Energy 49 (2013) 32–46.

[10] S. Yildiz, D.C. Groeneveld, Diameter effects on supercritical heat transfer, Int Commun Heat Mass 54 (2014) 27–32.

[11] Y.Y. Bae, H.Y. Kim, Convective heat transfer to CO_2 at a supercritical pressure flowing vertically upward in tubes and an annular channel, Exp. Therm. Fluid Sci. 33 (2009) 329–339.

[12] Y.Y. Bae, Mixed convection heat transfer to carbon dioxide flowing upward and downward in a vertical tube and an annular channel, Nucl. Eng. Des. 241 (2011) 3164–3177.

[13] R.B. Duffey, I.L. Pioro, Experimental heat transfer of supercritical carbon dioxide flowing inside channels, Nucl. Eng. Des. 235 (2005) 913–924.

[14] D. Huang, Z. Wu, B. Sunden, W. Li, A brief review on convection heat transfer of fluids at supercritical pressure in tubes and the recent progress, Appl. Energy 162 (2016) 494–505.

[15] D.E. Kim, M.H. Kim, Experimental study of the effects of flow acceleration and buoyancy on heat transfer in a supercritical fluid flow in a circular tube, Nucl. Eng. Des. 240 (2010) 3336–3349.

[16] S.H. Liu, Y.P. Huang, G.X. Liu, J.F. Wang, L.K.H. Leung, Improvement of buoyancy and acceleration parameters for forced and mixed convective heat transfer to supercritical fluids flowing in vertical tubes, Int. J. Heat Mass Tran. 106 (2017) 1144–1156.

[17] J.K. Kim, H.K. Jeon, J.Y. Yoo, J.S. Lee, Experimental Study on heat transfer characteristics of turbulent supercritical flow in vertical circular/non-circular tubes, The 11th International Topical Meeting on Nuclear Reactor Thermal-Hydraulics, 2005 Oct 2 − 6 (Avignon, France).

[18] K. Yamagata, K. NishmawaI, S. Hasegawa, T. Fujii, S. Yoshida, Forced convective heat transfer to supercritical water flowing in tubes, Int. J. Heat Mass Tran. 15 (1972) 2575–2593.

[19] J.D. Jackson, Fluid flow and convective heat transfer to fluids at supercritical pressure, Nucl. Eng. Des. 264 (2013) 24–40.

[20] Q. Zhang, H. Li, X. Kong, et al., Special heat transfer characteristics of supercritical CO2 flowing in a vertically-upward tube with low mass flux, Int. J. Heat Mass Tran. 122 (2018) 469–482.

[21] Q. Zhang, H. Li, X. Lei, et al., Study on identification method of heat transfer deterioration of supercritical fluids in vertically heated tubes, Int. J. Heat Mass Tran. 127 (2018) 674–686.

[22] P.K. Kundu, I.M. Cohen, D.R. Dowling, Fluid Mechanics, fifth ed., Elsevier, Amsterdam, 2012.

[23] S.G. Kandlikar, Heat transfer mechanisms during flow boiling in micro channels, J. Heat Tran. 126 (2004) 8–16.

[24] J.L. Xu, S. Shen, Y.H. Gan, Y.X. Li, W. Zhang, Q.C. Su, Transient flow pattern based microscale boiling heat transfer mechanisms, J. Micromech. Microeng. 15 (2005) 1344–1361.

[25] N.T. Rao, A.N. Oumer, U.K. Jamaludin, State − of − the − art on flow and heat transfer characteristics of supercritical CO_2 in various channels, J. Supercrit. Fluids 116 (2016) 132–147.

[26] L.F. Cabeza, A.D. Gracia, A.I. Fernández, M. Fari, Supercritical CO_2 as heat transfer fluid: a review, Appl. Therm. Eng. 125 (2017) 799–810.

[27] H. Hagi, T. Neveux, Y.L. Moullec, Efficiency evaluation procedures of coal-fired power plants with CO_2 capture, cogeneration and hybridization, Energy 91 (2015) 306–323.

[28] Y. Yang, W.G. Bai, Y.M. Wang, Y.F. Zhang, H.Z. Li, M.Y. Yao, et al., Coupled simulation of the combustion and fluid heating of a 300 MW supercritical CO_2 boiler, Appl. Therm. Eng. 113 (2017) 259–267.

[29] H.Y. Kim, H. Kim, J.H. Song, B.H. Cho, Y.Y. Bae, Heat transfer test in a vertical tube using CO_2 at supercritical pressures, J. Nucl. Sci. Technol. 44 (2007) 285–293.

[30] H. Zahlan, D. Groeneveld, S. Tavoularis, Measurements of convective heat transfer to vertical upward flows of CO_2 in circular tubes at near-critical and supercritical pressures, Nucl. Eng. Des. 289 (2015) 92–107.

[31] Y.Y. Bae, H.Y. Kim, D.J. Kang, Forced and mixed convection heat transfer to supercritical CO_2 vertically flowing in a uniformly-heated circular tube, Exp. Therm. Fluid Sci. 34 (2010) 1295–1308.

[32] D.E. Kim, M.H. Kim, Experimental investigation of heat transfer in vertical upward and downward supercritical CO_2 flow in a circular tube, Int. J. Heat Fluid Flow 32

(2011) 176–191.

[33] K. Jiang, An Experimental Facility for Studying Heat Transfer in Supercritical Fluids. PhD Thesis, Mechanical Engineering, Ottawa-Carleton Institute for Mechanical and Aerospace Engineering, 2015.

[34] H.Y. Kim, H. Kim, D.J. Kang, J.H. Song, Y.Y. Bae, Experimental investigations on heat transfer to CO_2 flowing upward in a narrow annulus at supercritical pressure,

Nucl Eng Technol 40 (2007) 155–162.

[35] R.N. Xu, F. Luo, P.X. Jiang, Buoyancy effects on turbulent heat transfer of supercritical CO_2 in a vertical mini-tube based on continuous wall temperature measurements, Int. J. Heat Mass Tran. 110 (2017) 576–586.

[36] B.S. Shiralkar, P. Griffith, Deterioration in heat transfer to fluids at supercritical pressures and high heat fluxes, J. Heat Transfer Trans. ASME 91 (1) (1969) 27–36.